Raman Thermometry Measurements and Thermal Simulations for MEMS Bridges at Pressures From 0.05 Torr to 625 Torr

Leslie M. Phinney[1]
e-mail: lmphinn@sandia.gov

Justin R. Serrano

Edward S. Piekos

John R. Torczynski

Michael A. Gallis

Allen D. Gorby

Engineering Sciences Center,
Sandia National Laboratories,
P.O. Box 5800,
Albuquerque, NM 87185-0346

This paper reports on experimental and computational investigations into the thermal performance of microelectromechanical systems (MEMS) as a function of the pressure of the surrounding gas. High spatial resolution Raman thermometry was used to measure the temperature profiles on electrically heated, polycrystalline silicon bridges that are nominally 10 μm wide, 2.25 μm thick, and either 200 μm or 400 μm long in nitrogen atmospheres with pressures ranging from 0.05 Torr to 625 Torr (6.67 Pa–83.3 kPa). Finite element modeling of the thermal behavior of the MEMS bridges is performed and compared with the experimental results. Noncontinuum gas effects are incorporated into the continuum finite element model by imposing temperature discontinuities at gas-solid interfaces that are determined from noncontinuum simulations. The results indicate that gas-phase heat transfer is significant for devices of this size at ambient pressures but becomes minimal as the pressure is reduced below 5 Torr. The model and experimental results are in qualitative agreement, and better quantitative agreement requires increased accuracy in the geometrical and material property values. [DOI: 10.1115/1.4000965]

Keywords: Raman thermometry, MEMS, finite element heat conduction simulations, noncontinuum gas-phase heat-transfer model, low-pressure effects, suspended microbridge

1 Introduction

The environmental conditions inside a packaged MEMS device dictate its performance and long-term reliability. Reducing packaging pressures below ambient decreases gas damping effects and gas-phase heat transfer and often is required to achieve the desired sensitivity for MEMS accelerometers, gyroscopes [1], ultrasonic sensors [2], infrared sensors [3], and bolometers [4]. Packaging microsystem devices at pressures lower than atmospheric dramatically affects their thermal performance since energy transfer to the environment is substantially reduced as the pressure is reduced.

In order to predict the performance and reliability of packaged MEMS devices, validated models of microsystems in varying environments are needed. Models of thermal performance of MEMS at varying pressures have been developed that account for noncontinuum gas-phase heat transfer at low pressures [5]; however, direct, spatially resolved, temperature measurements of MEMS structures in varying pressures were not available to validate the model results. Temperature measurements on MEMS at varying pressures are very challenging to obtain due to device sizes and access for diagnostic techniques. Lee et al. [6] used Raman thermometry to calibrate the temperature of a microcantilever heater with the dissipated electrical power at atmospheric pressure in air. They then measured the power dissipated as a function of pressure in air from 10^{-5} mbar to 10^{3} mbar and in helium from 10^{-3} mbar to 10^{3} mbar when the heater was operated at 673 K (1 mbar = 0.75 Torr = 100 Pa).

This study was undertaken to advance the understanding of thermal performance of packaged MEMS by experimentally and computationally determining temperature profiles at varying pressures on microbridges fabricated using sacrificial surface micromachining. The experimental methods are described, including the polycrystalline silicon (polysilicon) test structures, packaging of the test samples inside a Linkam stage, the gas control system used to vary the nitrogen atmosphere from 0.05 Torr (6.67 Pa) to ambient pressure, and Raman thermometry. Next, details for the numerical simulations are presented, including the noncontinuum gas model, material properties, and model geometry. The experimental and computational results are compared, and the effects of the environment on the thermal performance of a MEMS suspended bridge structure are discussed.

2 Test Structures

The SUMMiT V™ process [7,8] involves four structural *n*-type (phosphorous) polysilicon layers with a fifth layer as a ground plane. The polysilicon layers are separated by sacrificial oxide layers that are etched away during the final release step. The two topmost layers, Poly3 and Poly4, are nominally 2.25 μm in thickness, while the bottom two, Poly1 and Poly2, are nominally 1.0 μm and 1.50 μm in thickness, respectively. The ground plane, Poly0, is 0.30 μm in thickness and lies above a 0.80 μm layer of silicon nitride and a 0.63 μm layer of SiO_2. The sacrificial oxide layers between the structural layers are each roughly 2.0 μm thick.

Test structures used for the present study are fabricated from the Poly4 layer and are nominally 2.25 μm thick, 10 μm wide, and 200 μm or 400 μm long. The fixed-fixed bridges end at bond pads, layered structures that mechanically anchor the beam to the substrate and provide a location for wire bonding to the package. The wires are bonded to a 0.70 μm layer of aluminum

[1]Corresponding author.

Contributed by the Heat Transfer Division of ASME for publication in the JOURNAL OF HEAT TRANSFER. Manuscript received May 18, 2009; final manuscript received December 10, 2009; published online April 28, 2010. Assoc. Editor: He-Ping Tan.

This material is declared a work of the US Government and is not subject to copyright protection in the United States. Approved for public release; distribution is unlimited.

Downloaded From: https://heattransfer.asmedigitalcollection.asme.org on 06/29/2019 Terms of Use: http://www.asme.org/about-asme/terms-of-use

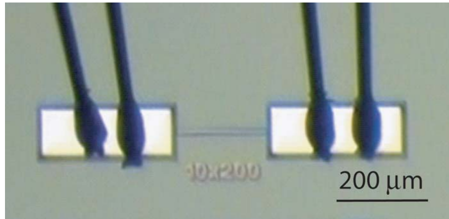

Fig. 1 Optical microscope image of a 10 μm wide × 200 μm long test structure fabricated using the SUMMiT V™ process. The bond pads are 100 μm wide and 300 μm long. Two wires bonded to each bond pad are visible in the image. The connections to the package are outside of the image.

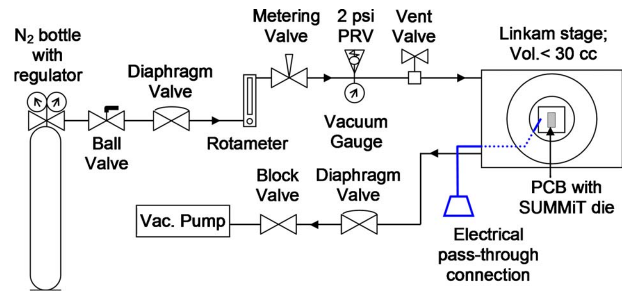

Fig. 2 Schematic of the layout of the vacuum and gas supply system for the experiments

that is deposited on top of the bond pad. Figure 1 is an image of a 10 μm wide, 200 μm long test structure with the bond pads and bond wires visible.

3 Experimental Methods

Temperature measurements were obtained with micro-Raman spectroscopy [9] using a Renishaw inVia Raman microscope. The microscope uses a 180 deg backscattering geometry and a 488 nm Ar^+ laser as the probe that produces a diffraction-limited spot of 560 nm in diameter when focused by a 50×, 0.50-numerical-aperture objective. The actual measurement diameter within the sample is larger, 1.70 μm, because of spreading of the probe laser within the sample. The Raman signal from the sample surface is collected through the objective, dispersed by a grating spectrograph, and detected with a back-side illuminated, thermoelectrically cooled charge coupled device (CCD) camera (Pixis 1024B, Princeton Instruments, Trenton, NJ). Dispersion of the Raman signal at the CCD is 0.57 cm^{-1}/pixel.

Laser power at the sample is attenuated to 65 μW to minimize localized heating of the sample that would otherwise introduce a bias into the temperature measurement. Minimal heating of the sample is confirmed by obtaining Raman spectra at decreasing laser powers from a room-temperature SUMMiT sample until no change in the Raman peak position was observed. Using scaling arguments presented by Kearney et al. [9], the power deposited on the probed location, assuming full absorption and a sample thermal conductivity of 30 W/m K (equivalent to SUMMiT polysilicon at 523 K), would amount to a temperature increase of 1.3 K; considering a silicon surface reflectivity of 39% [10], this value is likely closer to 0.8 K.

In the Raman process, photons from the incident probe light source interact with the optical phonon modes of the irradiated material and are scattered to higher (anti-Stokes) or lower (Stokes) frequencies from the probe line frequency. In the case of silicon and polysilicon, the scattered Raman light arises from the triply degenerate optical phonon at the Brillouin zone center. The resulting spectrum for the Stokes (lower frequency) Raman response has a single narrow peak at approximately 520 cm^{-1} from the laser line frequency at room temperature. Increases in temperature affect the frequency, lifetime, and population of the phonon modes coupled to the Raman process, leading to changes in the Raman spectra, namely, a shift in the peak position and broadening of the Raman peak. Both metrics are practical for temperature mapping of MEMS. However, while peak width is sensitive only to surface temperature, peak position is sensitive to both stress and temperature [9,11].

For thermometry of the test beams under varying-pressure conditions, a Linkam temperature-controlled thermal stage fitted with vacuum ports was used. A diagram of the layout of the vacuum system is shown in Fig. 2. The system used ultra-high-purity nitrogen gas as the purge gas and permitted control of the pressure inside the stage from ambient (nominally 625 Torr ± 10 Torr) to 0.010 Torr measured with a BOC Edwards Pirani gauge. The flow rate of nitrogen into the stage was maintained at 20 cc/min for pressures above 0.05 Torr, and at 6 cc/min for a pressure setting of 0.05 Torr. With a chamber volume of ~30 cc, the gas exchange rate inside the chamber is 1.5 min at all pressures, except for 0.05 Torr where it is about 5 min.

To provide electrical power to the test devices, the SUMMiT die was packaged on a printed circuit board (PCB) to which wire leads were soldered. Each bond pad on the beam structure is wire-bonded to two separate connections on the PCB to allow for four-point sensing of the voltage. Quick-disconnect connectors were used inside the stage to allow for easy exchange of parts. The PCB was placed in the center of a quartz crucible inside the stage and held in place with a vacuum-compatible carbon tape (Fig. 3). The heating ability of the stage was used to heat the sample to a temperature of 300–310 K to ensure a consistent substrate temperature for the measurements. The devices were powered with a Keithley 2400 source meter in a four-point sensing configuration, where the current is flowed through the outside connections and the voltage is measured across the inner ones.

Prior to performing the measurements on the test structures, a temperature calibration of the Raman response from the Poly4 layer was obtained by placing a die in a second temperature-controlled hot stage and acquiring Raman data over a temperature range 300–700 K. The sample used in the calibration was from the same fabrication run as those used in the validation measurements but was a different die. A Voigt function, which captures both the Lorentzian Raman line shape and the Gaussian instrument function, is fitted to the Raman spectral data to extract both the center position Ω and the full width at half maximum (FWHM) Γ_{Raman} of the Raman peak [9]. At different temperatures in the calibration

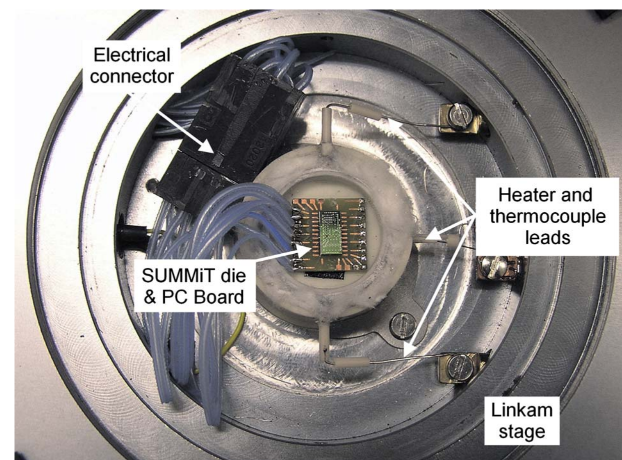

Fig. 3 Close-up of the packaged SUMMiT die inside the Linkam stage. The silicon die in the center of the square printed circuit board piece is 3.6 mm wide × 6.3 mm long.

Downloaded From: https://heattransfer.asmedigitalcollection.asme.org on 06/29/2019 Terms of Use: http://www.asme.org/about-asme/terms-of-use

range, six spectra are acquired from the sample and fitted, and the extracted peak position and peak width are then averaged and plotted as a function of temperature.

The data are then fitted to a calibration function that correlated the observed change in the Raman spectra to temperature. For the Raman peak position, the correlation is linear and is described by the expression

$$\Omega = \frac{\partial \Omega}{\partial T} T + \Omega_o \quad (1)$$

where $\partial\Omega/\partial T = -0.0239 \pm 0.00018\ \text{cm}^{-1}/\text{K}$, T is in K, and $\Omega_o = 527.314\ \text{cm}^{-1}$. For the Raman peak width (FWHM), the correlation is quadratic with temperature and is given by the expression

$$\Gamma_{\text{Raman}} = A(T+B)^2 + C \quad (2)$$

where $A = 5.129 \times 10^{-6}\ \text{cm}^{-1}/\text{K}^2$, $B = 407.213$ K, and $C = 1.608\ \text{cm}^{-1}$. Since the Poly4 fixed-fixed beams used in this study (Fig. 1) are anchored at both ends, thermal expansion during heating is constrained, and the beams are placed under compressive stress during their operation. For this reason, peak width is used as the metric for the test, and sample temperature is extracted using Eq. (2).

Two devices were tested for the validation measurements: a $10 \times 200\ \mu\text{m}^2$ beam and a $10 \times 400\ \mu\text{m}^2$ beam. The Raman temperature measurements were taken under five different pressure conditions (625 Torr, 50 Torr, 5 Torr, 0.5 Torr, and 0.05 Torr) for both geometries. The electrical currents used to power the devices were chosen so as to provide relatively consistent peak temperatures over the various pressures. The $10 \times 200\ \mu\text{m}^2$ beam was tested under two current conditions that would provide peak temperatures of 400–450 K and 600 K, respectively; the $10 \times 400\ \mu\text{m}^2$ beam was powered to provide a peak temperature of 450–500 K.

Error bars were calculated that represent the collective error in the measurement from the principal sources of uncertainty in the measurement, which are the accuracy of the peak width extraction and the error resulting from the temperature calibration. The peak width extraction through the curve fit was the largest source of uncertainty, with an uncertainty of ± 6.58 K over the temperature range explored in the samples, as determined by taking multiple spectra at a fixed temperature during the calibration. The error contribution from the temperature calibration curve (Eq. (2)) is ± 4.66 K. The contribution of system drift, although accounted for during the measurements by taking data from an unheated reference, is only ± 0.03 K for peak width measurements.

An additional source of uncertainty is the variation in the pressure of the system. For the system discussed above, the uncertainty in the pressure control is $\pm 1\%$ of the full scale for pressures below 100 Torr and 1 Torr for higher pressures. Here, full scale for the vacuum gauge is taken to be the next-highest power of 10 in Torr from the pressure reading (i.e., 10 Torr full scale for a 5 Torr pressure, with an uncertainty of ± 0.1 Torr). The corresponding temperature fluctuation due to these pressure variations is estimated to be no more than ± 3.5 K for all pressures and conditions based on the fluctuations observed in the voltage drop across the sample with the observed pressure fluctuations.

Assuming that these uncertainties are uncorrelated yields an uncertainty for the peak-width-based temperature measurement of ± 8.79 K. This total uncertainty is slightly lower than previously reported by Beechem et al. [11], namely, ~ 9 K rather than ~ 11 K, because of the increased number of acquisitions used and the increased signal level used.

4 Numerical Methods

Electrothermal simulations were performed for the experimentally investigated devices using CALORE. CALORE [12,13] is a massively parallel finite element method (FEM) thermal analysis application developed within the SIERRA analysis-code framework at Sandia National Laboratories under the Advanced Simulation and Computing (ASC) program of the National Nuclear Security Administration (NNSA). The present investigation builds on earlier research that used CALORE to investigate noncontinuum heat transfer in microsystems [14] by simulating a beam under user-specified volumetric heating. In the current work, steady-state heat conduction in the test structure and the surrounding gas is simulated, including thermal resistance due to the multilayer bond pads (detailed in Ref. [15]) and nonuniform Joule heating from a specified current due to a temperature-dependent electrical resistance.

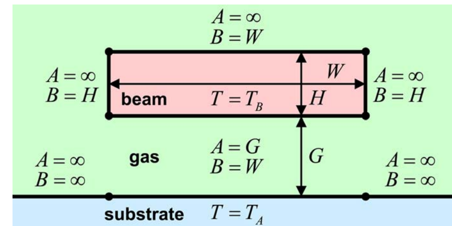

Fig. 4 Schematic of the gas heat-transfer model

Electrical heating problems are modeled in CALORE by loosely coupling two calculations: one that solves for the voltage distribution, and one that solves for the temperature distribution. The electrical calculation determines the Ohmic heating, which is then provided as a volumetric heat source in the temperature calculation. The temperature calculation determines the temperature distribution, which is then provided to the electrical calculation to calculate the temperature-dependent electrical conductivity.

Thermal MEMS devices fabricated using the SUMMiT V process have certain geometric features in common. These devices are composed of planar layers of uniform thickness that are separated from adjacent layers by gaps of uniform thickness, with perpendicular sides. Moreover, these devices employ long beams of rectangular cross section. Because of the large thermal conductivity of crystalline and polycrystalline silicon, the temperature of a heated beam is nearly uniform in each cross section, although the temperature can vary significantly along the length. Similarly, the substrate beneath a heated beam remains very nearly at the ambient temperature.

Extending the model of Gallis et al. [5] and based on the above observations, the paradigmatic microscale geometry for noncontinuum gas-phase heat-transfer model development is illustrated in Fig. 4. A beam of infinite length (out of the page) and finite width W and finite height (thickness) H is separated by a gap of uniform constant height G from a planar substrate of infinite length (out of the page) and infinite width. The beam cross section is at uniform constant elevated temperature T_B, and the substrate is at uniform constant ambient temperature T_A. The space between the beam and the substrate is filled with gas at uniform constant pressure $p = p_{\text{amb}}$ and spatially varying temperature T that approaches the ambient temperature T_A far from the beam.

The above geometry can be further broken down into a series of line segments of finite or infinite breadth that face either an identical parallel line segment at a fixed separation or else unbounded space. Thus, each line segment in Fig. 4 has a finite or infinite breadth B (the distance between its end points) and a finite or infinite separation A from a parallel segment. In Fig. 4, the separation A and the breadth B are given for each of the seven line segments in terms of the geometric lengths.

In the gas region, steady heat conduction is simulated using the temperature-dependent gas thermal conductivity K. When heat flows across a gas-solid interface, noncontinuum gas behavior causes the gas and solid temperatures to differ. The normal heat flux q can be related to the temperature difference across the interface ΔT in terms of a heat-transfer coefficient h [5] as follows:

Downloaded From: https://heattransfer.asmedigitalcollection.asme.org on 06/29/2019 Terms of Use: http://www.asme.org/about-asme/terms-of-use

Table 1 Aluminum, silicon dioxide, and silicon nitride properties (300 K)

Quantity	Al	Oxide	Nitride
Thermal conductivity (W/m K)	235	1.4	3.2
Electrical resistivity (Ω m)	0.028	-	-

$$q = h\Delta T \tag{3}$$

This expression provides a convenient means for expressing a noncontinuum effect in the continuum FEM simulations. At a boundary between gas and a solid, a temperature discontinuity can be maintained while satisfying conservation of energy by enforcing continuity of the flux. The magnitude of this discontinuity, which is assumed dependent solely on the gas conditions, is set by the heat-transfer coefficient h.

The following functional form of the heat-transfer coefficient is applied at all gas-solid interfaces shown in Fig. 4:

$$h = \left(1 + \frac{\zeta}{4}\right)\left(\frac{\sigma}{S_1 S_2}\right)\left(\frac{p\bar{c}}{T}\right) \tag{4}$$

$$S_1 = 2 - \sigma + \frac{\sigma}{1 + c_4(B/A) + c_5(B/\lambda)} \tag{5}$$

$$S_2 = 1 + \frac{c_1\sigma}{1 + c_2(\lambda/A) + c_3(\lambda/B)} \tag{6}$$

$$\lambda = \frac{2\mu}{\rho\bar{c}} \tag{7}$$

$$\bar{c} = \sqrt{\frac{8k_B T}{\pi m}} \tag{8}$$

and

$$\rho = \frac{mp}{k_B T} \tag{9}$$

Here, ζ is the number of molecular internal energy modes (2 for nitrogen), σ is the thermal accommodation coefficient (the probability between 0 and 1 that a gas molecule exchanges thermal energy when it reflects from a solid surface), S_1 and S_2 are order-unity dimensionless factors, A and B are the separation and breadth of a line segment, $\bar{c}$ is the molecular mean thermal speed, λ is the molecular mean free path, μ is the viscosity, ρ is the mass density, m is the molecular mass, k_B is the Boltzmann constant, and c_1–c_5 are positive dimensionless parameters that enable S_1 and S_2 to behave correctly in limiting regimes. The above functional form reproduces known gas heat-transfer behavior in the near-continuum and free-molecular regimes for parallel-plate and isolated-body geometries [5]. The parameters c_1–c_5 control the transitions between various limiting regimes. For nitrogen, their values are c_1=0.167, c_2=0.599, c_3=1.23, c_4=0.32, and c_5=1.02. Temperature-dependent thermophysical properties for nitrogen can be found in Ref. [16].

The test structure contains four materials: polycrystalline silicon (polysilicon), silicon dioxide (oxide), silicon nitride (nitride), and aluminum. The thermophysical properties of the materials other than polysilicon are obtained from published values and listed in Table 1. These materials are deposited using reasonably standard processes, and the effects of these processes on the quantities of interest in this work are reasonably small. Resistivity values are not provided for oxide and nitride because they are excluded from the electrical model.

The thermophysical properties for polysilicon vary strongly with processing conditions and with temperature and are critical

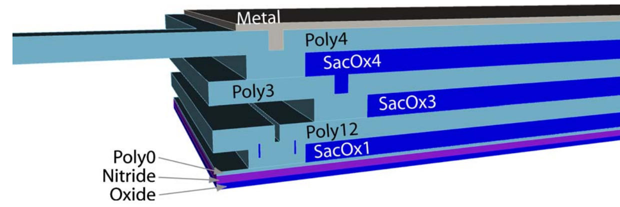

Fig. 5 Cross section showing the layers in the bond pad and base of the beam. Layer thicknesses are specified in Table 2.

to the current work. Thus, efforts were made to ensure appropriate values through comparisons with earlier measurements on SUMMiT polysilicon for the electrical resistivity r_s and the thermal conductivity K_s [15,17]. The resistivity values were found to be represented well by the following linear equation in temperature, where the temperature T is in K and the resistivity r_s is in Ω μm [18]:

$$r_s = 0.0232T + 13.6997 \tag{10}$$

The functional form of the thermal conductivity was determined from earlier measurements, and the offset was adjusted by performing simulations for a high-power, low-pressure, 10 ×200 μm^2 beam for which the gas-phase transport is not significant (10.75 mW and 0.05 Torr). The resultant thermal conductivity is given as follows, where T is in K and K_s is in W/m K [18]:

$$K_s = \frac{1}{0.0066 + 0.00116(0.03T - 2)} - 6.5 \tag{11}$$

While the heated bridge portion of the test structure has a very simple geometry, the layers and geometry of the anchors are fairly complex [15]. These anchor points, also known as "bond pads" since the wires for electrical connections are bonded to them, have complex multilayer structures due to constraints imposed by the SUMMiT V manufacturing process. Because cross sections of the actual devices used in this work were not available, the geometry was built based on available computational models, with some input from measured quantities. The layer thicknesses were adjusted to bring the beam height above the substrate, 11.872 μm, into agreement with the interferometry measurements of the test structures used in the experiments. Figure 5 shows a cross section of a bond pad and base of a beam, and Table 2 lists the dimensions adopted for the computational model.

The gas heat conduction problem was solved on a mesh 100 μm wide and 50 μm tall. These dimensions were chosen by solving a steady-state, two-dimensional problem with a beam cross section held at 600 K. The domain boundaries were then placed such that the temperature gradient, and therefore the heat flux, fell below 1% of its magnitude at the beam surface at these locations, ensuring that placing insulating boundaries at these lo-

Table 2 Geometric dimensions used in CALORE computational model

Layer thickness	Model value (μm)	Other lengths	Model value (μm)
Thermal oxide	0.630	Beam length (short)	200.00
Silicon nitride	0.800	Beam length (long)	400.00
Poly0	0.300	Beam width (both)	9.65
SacOx1	2.000	Bond pad x width	100.00
Poly12	2.260	Bond pad y width	41.00
SacOx3	2.461	Gas domain y width	100.00
Poly3	2.320	Gas domain z height	50.00
SacOx4	2.461		
Poly4	2.330		
Metal	0.700		

Downloaded From: https://heattransfer.asmedigitalcollection.asme.org on 06/29/2019 Terms of Use: http://www.asme.org/about-asme/terms-of-use

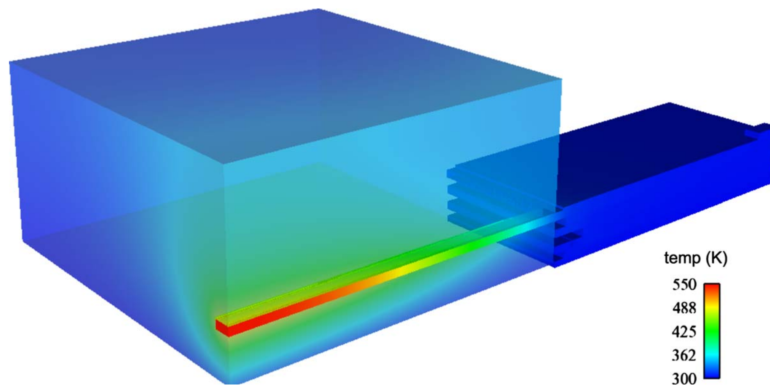

Fig. 6 Temperature field for a 200 μm long beam at 50 Torr (6.67 kPa) with an initial temperature of 304.15 K and operated at 12.41 mW with unity accommodation (Case 16)

cations would have little effect on the solution. The gas grid is truncated at the base of the beam because the temperature at this point is expected to be very near ambient, so there is little expected benefit in gridding between the layers at the forward edge of the bond pad.

Grids were constructed in three levels, with uniform refinement followed by localized refinement based on the gradient in voltage for the electrical grid. The coarse mesh contained 69,543, 244,665, and 959,916 elements for the electrical, solid, and gas grids, while the finest mesh contained 4,264,832, 15,472,640, and 35,318,496 elements. Most calculations were carried out on the medium grid, which contained 540,139, 1,941,115, and 4,436,064 elements. Computation times for the three grids for a typical calculation were 0.1 h, 1.3 h, and 5.9 h on 50 Infiniband-connected nodes of the Sandia "Thunderbird" cluster with two 3.6 GHz EM64T processors each. The typical calculation was for a 200 μm long beam at 50 Torr (6.67 kPa) with an initial temperature of 304.15 K and operated at 12.41 mW with a thermal accommodation coefficient of 0.3, the intermediate value considered. For this calculation, the temperature difference across the beam deviated from the finest grid value by 1.2% and 0.4% on the coarse and medium grids, respectively. The results computed on the medium grid are therefore very likely grid converged to well within the experimental error.

5 Results

Using the noncontinuum gas-phase heat-transfer model for the surface heat-transfer coefficient and the specified material properties and geometry, an example of typical model results for the temperature distribution in the beam and gas with an accommodation coefficient of unity is shown in Fig. 6 for a 200 μm long beam at 50 Torr with an initial temperature of 304.15 K and operated at 12.41 mW. Several features are visible in these results. First, the beam temperature is somewhat higher than that of the adjacent gas. This is a consequence of the noncontinuum gas-solid boundary condition. Second, the highest temperature, and most of the gas-phase heat transfer to the substrate, occurs at the beam center because the ends are cooled by conduction through the bond pad.

The combined gas-solid heat-transfer model described in Sec. 4 is applied to compute temperature profiles corresponding to the conditions for which the temperature profiles were measured. Figures 7 and 8 show the calculated and measured temperature profiles for the 200 μm and 400 μm beams, respectively. Each plot in each figure contains all model and experimental temperature profiles for the same beam length and the same gas pressure. The measured data are labeled by beam length, pressure, power, and measurement run or case number. Each 200 μm plot contains temperature profiles for two powers ("high" and "low"), whereas each 400 μm plot contains temperature profiles for only one power ("low"). The high-power and low-power conditions produce maximum temperatures of ~600 K and ~450 K, respectively. The 625 Torr, 200 μm plot is divided into two separate plots for reasons that will be discussed. The 625 Torr, 200 μm plot in Fig. 7(*e*) contains an additional power ("medium"). The colors red, green, and blue denote high, medium, and low, respectively.

The temperature measurements indicate that increasing the pressure by a factor of 10 from 0.05 Torr to 0.5 Torr hardly changes the temperature profiles and the corresponding powers. This is consistent with the results of Lee et al. [6] for which the dissipated power from a microcantilever heater at 673 K was fairly constant below 1 mbar (0.75 Torr) in air and helium atmospheres. This observation indicates that gas-phase heat transfer is negligible compared with solid-phase heat transfer at these low pressures. When the pressure is increased to 5 Torr, the power must be increased by about 4% to keep the peak of the temperature profile around 600 K, so gas-phase heat transfer is about 4% of solid-phase heat transfer at 5 Torr. A similar comparison indicates that gas-phase heat transfer is about 15% and 31% of solid-phase heat transfer at gas pressures of 50 Torr and 625 Torr, respectively. Thus, gas-phase heat transfer is significant for devices of this size at ambient pressure but becomes minimal as the pressure is reduced.

For each combination of beam length, gas pressure, and power, three model temperature profiles are presented in Figs. 7 and 8, corresponding to accommodation coefficients of 1.0, 0.3, and 0.0. A value of 1.0 produces the maximum gas heat transfer possible, a value of 0.0 produces no gas heat transfer, and the intermediate value of 0.3 is a low value compared with measurements [19,20].

As the pressure increases from 0.05 Torr to 0.5 Torr and to 5 Torr, the three model profiles for each condition are seen to separate, which indicates the increasing importance of gas heat transfer as the pressure increases although gas heat transfer is not large yet. The high-power model and experimental profiles in Figs. 7(*a*)–7(*c*) agree well. However, this agreement is not unexpected because the thermal conductivity model is calibrated to match the 0.05 Torr high-power profile and because gas heat transfer is still quite small below 5 Torr. For the low-power profiles in these plots, the model again slightly overpredicts the temperature rise near the beam ends and also slightly underpredicts the maximum temperature rise by a progressively greater amount as the pressure is increased.

As the pressure increases to 50 Torr, the agreement between the model and experimental profiles deteriorates, particularly for the low-power cases (Fig. 7(*d*)). At this pressure, the mean free path of gas molecules is about 1 μm, and is comparable to the beam thickness. This is the regime in which the gas-solid heat-transfer-

Downloaded From: https://heattransfer.asmedigitalcollection.asme.org on 06/29/2019 Terms of Use: http://www.asme.org/about-asme/terms-of-use

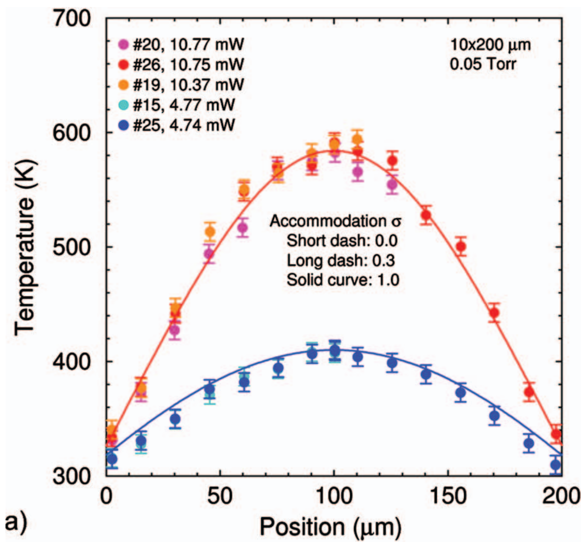

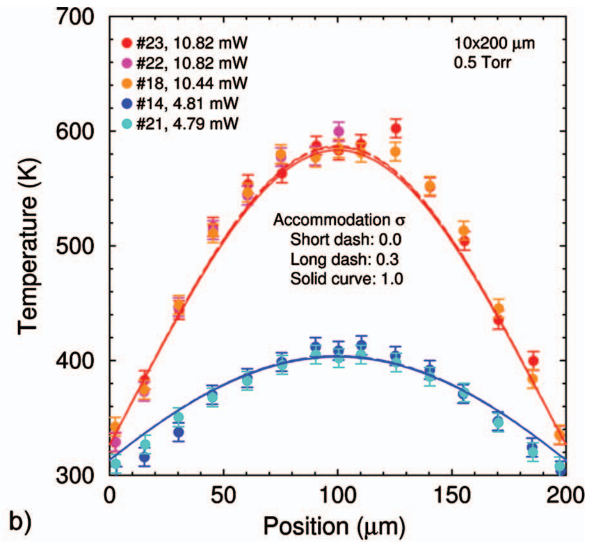

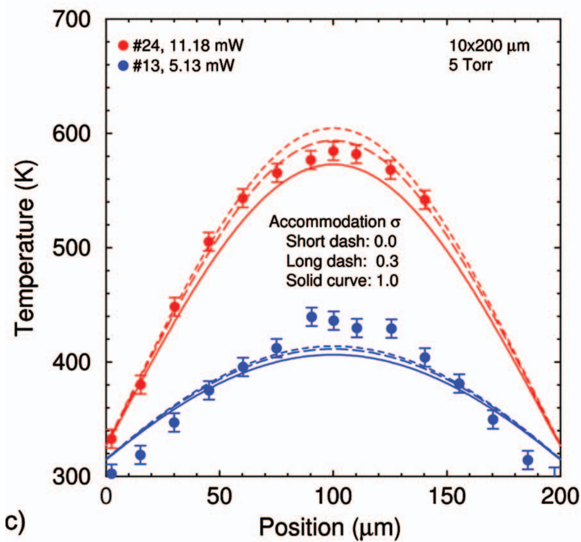

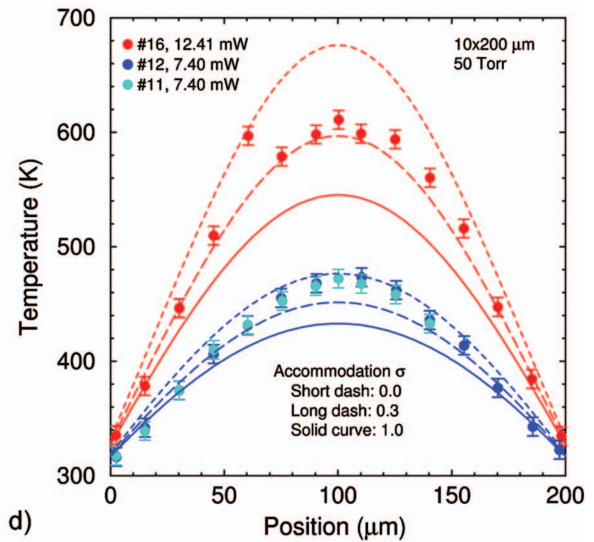

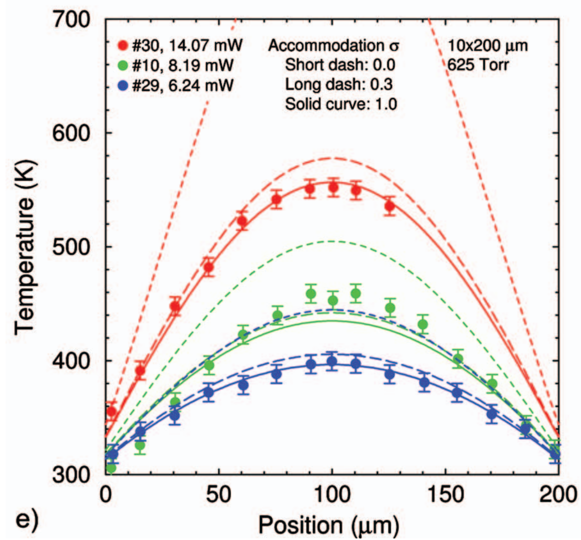

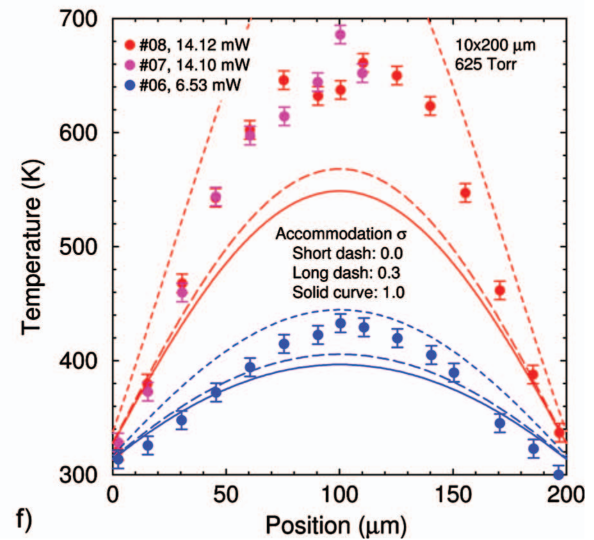

Fig. 7 Comparison of experimental (symbols) and simulation (lines) temperature profiles on 200 μm long beams at 0.05–625 Torr (6.67 Pa–83.3 kPa)

Downloaded From: https://heattransfer.asmedigitalcollection.asme.org on 06/29/2019 Terms of Use: http://www.asme.org/about-asme/terms-of-use

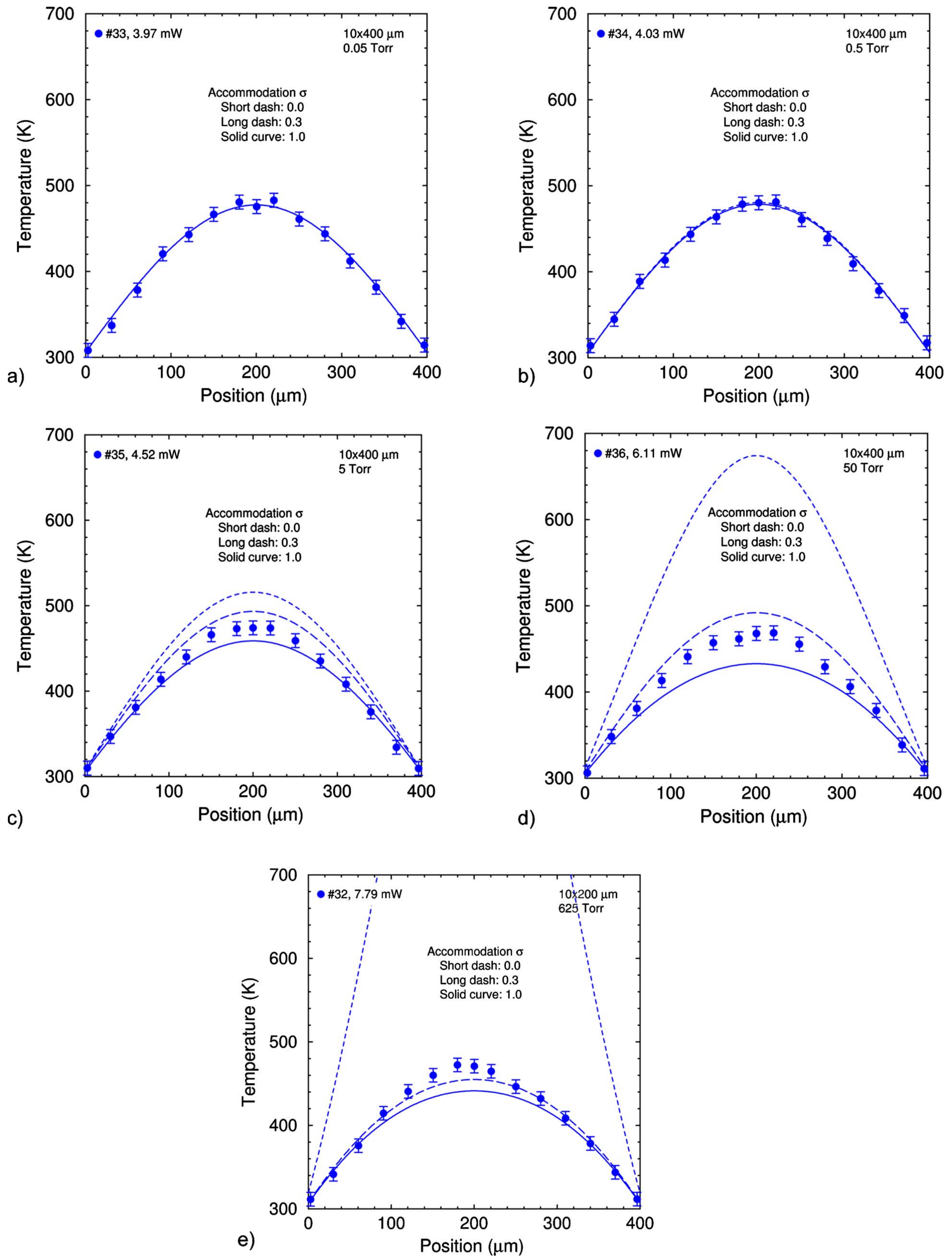

Fig. 8 Comparison of experimental (symbols) and simulation (lines) temperature profiles on 400 μm long beams at 0.05–625 Torr (6.67 Pa–83.3 kPa)

Downloaded From: https://heattransfer.asmedigitalcollection.asme.org on 06/29/2019 Terms of Use: http://www.asme.org/about-asme/terms-of-use

coefficient model is expected to be least accurate. However, the differences are more than what would be expected based on the comparisons of molecular and FEM gas simulations. An accommodation coefficient of 0.3 would represent the high-power profile well and the low-power profile marginally, but this value is much lower than expected [19,20].

The thermal conductivity of polysilicon depends strongly on the crystal structure, which can vary between processing runs and change over time, especially at high temperatures. Thus, the temperature-dependent thermal conductivity in Eq. (11) includes a temperature-independent offset selected to make the red model curve pass through the red symbols in Fig. 7(*a*). This high-power low-pressure case was used because the full temperature range is accessed and the gas heat transfer is essentially zero so that only the solid properties are important. This "calibrated" temperature-dependent thermal conductivity (Eq. (11)) lies within the reported measurement uncertainty (15%) and is used without modification in all the simulations.

This calibration approach can be assessed to some degree by examining the low-power low-pressure temperature profiles (blue values, Fig. 7(*a*)). The model predicts the maximum temperature rise reasonably well but systematically overpredicts the temperature rise near the beam ends. This difference is not as visible in the two low-pressure 400 μm cases (low-power) of Figs. 8(*a*) and 8(*b*), for which the simulation curves lie within the error bars for the entire temperature distribution.

Experimental artifacts are clearly visible in the two 625 Torr plots in Figs. 7(*e*) and 7(*f*). The maximum temperature rises of the profiles in Fig. 7(*f*) are roughly 40% larger than the corresponding values of the profiles in Fig. 7(*e*) despite the fact that the powers are almost identical. The experimental results in Fig. 7(*f*) are the first three data sets among those reported that were collected: Cases 6, 7, and 8. Given the difference in these data sets, something happened between Case 8 and Case 10 that altered the thermal behavior of the beams significantly and permanently.

At a pressure of 625 Torr (ambient), the experimental profiles are divided into two groups: Cases 10 and 29–30 (Fig. 7(*e*)) and Cases 6–8 (Fig. 7(*f*)). The model and experimental profiles agree well for Cases 10 and 29–30 but differ for Cases 6–8. Again, this is not a defect of the model; rather, the experimental results differ significantly between themselves. Since the model is calibrated using Case 26, it is reasonable that the model agrees more closely with the later cases than with the earliest cases.

For most low-power profiles in Fig. 7, the model overpredicts the experimental temperatures near the beam ends and underpredicts the experimental maximum temperature rise. One possibility suggested by this observation is that the experimental thermal conductivity is larger at ambient temperature but decreases more rapidly with increasing temperature than the thermal conductivity used in the model.

The model and experimental 400 μm temperature profiles are in reasonable agreement although the agreement degrades as the gas pressure is increased as seen in Fig. 8. These profiles are all low-power and are similar to those of the 200 μm beams.

6 Conclusions

This paper reports the first spatially resolved Raman temperature profiles for polysilicon MEMS, suspended 10 μm wide microbridges with lengths of 200 μm and 400 μm in nitrogen atmospheres at pressures varying from 0.05 Torr to 625 Torr (6.67 Pa–83.3 kPa). Temperature profiles are also computationally obtained using a finite element code, CALORE, with a heat-transfer coefficient at gas-solid surfaces derived from the noncontinuum gas-phase heat-transfer model. The experimental and simulation results indicate that at pressures below 0.5 Torr the gas-phase heat transfer is negligible compared with solid conduction. As the pressure increases above 0.5 Torr, the gas-phase heat transfer becomes more significant. For polysilicon MEMS structures at ambient pressures, gas-phase heat transfer significantly impacts the thermal performance. The measured and simulated temperature profiles are in qualitative agreement in the present study. Quantitative agreement between experimental and simulated temperature profiles requires accurate knowledge of temperature-dependent thermophysical properties' values, device geometries, and thermal accommodation coefficients.

Acknowledgment

Sandia is a multiprogram laboratory operated by Sandia Corporation, a Lockheed-Martin Co., for the U.S. Department of Energy's National Nuclear Security Administration under Contract No. DE-AC04-94AL85000.

Nomenclature

A = distance from one wall to the nearest parallel wall, m
B = distance from one corner to the other of finite-extent wall, m
A,B,C = constants in Eq. (2)
$\bar{c}$ = molecular mean thermal speed, m/s
c_1–c_5 = positive dimensionless parameters in Eqs. (5) and (6)
h = heat-transfer coefficient at gas-solid interface, $\mathrm{W/(m^2\,K)}$
k_B = Boltzmann constant, 1.380658×10^{-23} J/K
K = gas thermal conductivity, W/(m K)
K_s = solid thermal conductivity, W/(m K)
m = mass of gas molecules, kg
p = gas pressure, Pa
r_s = electrical resistivity, Ω μm
S_1,S_2 = factors in the heat-transfer coefficient h (unity or larger)
T = temperature, K
V = voltage, V

Greek Symbols

Γ_{Raman} = FWHM of the Raman peak, $\mathrm{cm^{-1}}$
ζ = number of internal energy modes of gas molecules (non-negative)
λ = mean free path of gas molecules, m
μ = gas viscosity, Pa s
ρ = gas mass density, $\mathrm{kg/m^3}$
σ = thermal accommodation coefficient (0–1)
Ω = center frequency of the Raman peak, $\mathrm{cm^{-1}}$
Ω_o = initial center frequency of the Raman peak, $\mathrm{cm^{-1}}$

References

[1] Kim, J.-S., Lee, S.-W., Jung, K.-D., Kim, W.-B., Choa, S.-H., and Ju, B.-K., 2008, "Quality Factor Measurement of Micro Gyroscope Structure According to Vacuum Level and Desired Q-Factor Range Package Method," Microelectron. Reliab., **48**, pp. 948–952.
[2] Xuecheng, J., Ladabaum, I., Degertekin, F. L., Calmes, S., and Khuri-Yakob, B. T., 1999, "Fabrication and Characterization of Surface Micromachined Capacitive Ultrasonic Immersion Transducers," J. Microelectromech. Syst., **8**(1), pp. 100–114.
[3] Eriksson, P., Andersson, J. Y., and Stemme, G., 1997, "Thermal Characterization of Surface-Micromachined Silicon Nitride Membranes for Thermal Infrared Detectors," J. Microelectromech. Syst., **6**(1), pp. 55–61.
[4] Nagapriya, K. S., Raychaudhuri, A. K., Jain, V. K., Jalwania, C. R., and Kumar, V., 2003, "Effect of Ambient on the Thermal Parameters of a Micromachined Bolometer," Appl. Phys. Lett., **82**(16), pp. 2721–2723.
[5] Gallis, M. A., Torczynski, J. R., and Rader, D. J., 2007, "A Computational Investigation of Noncontinuum Gas-Phase Heat Transfer Between a Heated Microbeam and the Adjacent Ambient Substrate," Sens. Actuators A, **134**(1), pp. 57–68.
[6] Lee, J., Wright, T. L., Abel, M. R., Sunden, E. O., Marchenkov, A., Graham, S., and King, W. P., 2007, "Thermal Conduction From Microcantilever Heaters in Partial Vacuum," J. Appl. Phys., **101**, p. 014906.
[7] MEMS Technologies Department, 2008, "SUMMiT V™ Five Level Surface Micromachining Technology Design Manual, Version 3.1a," Sandia Report No. SAND2008-0659P, Sandia National Laboratories, Albuquerque, NM.

Downloaded From: https://heattransfer.asmedigitalcollection.asme.org on 06/29/2019 Terms of Use: http://www.asme.org/about-asme/terms-of-use

[8] Sniegowski, J. J., and de Boer, M. P., 2000, "IC-Compatible Polysilicon Surface Micromachining," Annu. Rev. Mater. Sci., **30**, pp. 299–333.
[9] Kearney, S. P., Phinney, L. M., and Baker, M. S., 2006, "Spatially Resolved Temperature Mapping of Electrothermal Actuators by Surface Raman Scattering," J. Microelectromech. Syst., **15**(2), pp. 314–321.
[10] Aspnes, D. E., and Studna, A. A., 1983, "Dielectric Functions and Optical Parameters of Si, Ge, GaP, GaAs, GaSb, InP, InAs, and InSb From 1.5 to 6.0 eV," Phys. Rev. B, **27**(2), pp. 985–1009.
[11] Beechem, T., Graham, S., Kearney, S. P., Phinney, L. M., and Serrano, J. R., 2007, "Simultaneous Mapping of Temperature and Stress in Microdevices Using Micro-Raman Spectroscopy," Rev. Sci. Instrum., **78**(6), p. 061301.
[12] Bova, S. W., Copps, K. D., and Newman, C. K., 2006, "Calore: A Computational Heat Transfer Program, Volume 1: Theory Manual," Sandia Report No. SAND2006, Sandia National Laboratories, Albuquerque, NM.
[13] Calore Development Team, 2008, "Calore: A Computational Heat Transfer Program, Volume 2: User Reference Manual, Version 4.6," Sandia Report No. SAND2008-0098P, Sandia National Laboratories, Albuquerque, NM.
[14] Torczynski, J. R., Wong, C. C., Piekos, E. S., Gallis, M. A., Rader, D. J., and Bainbridge, B. L., 2005, "Modeling Microscale Heat Transfer Using Calore," Sandia Report No. SAND2005-5979, Sandia National Laboratories, Albuquerque, NM.
[15] Phinney, L. M., Piekos, E. S., and Kuppers, J. D., 2007, "Bond Pad Effects on Steady State Thermal Conductivity Measurement Using Suspended Micromachined Test Structures," ASME Paper No. IMECE2007-41349.
[16] White, F. M., 1984, *Heat Transfer*, Addison-Wesley, Reading, MA.
[17] Phinney, L. M., Kuppers, J. D., and Clemens, R. C., 2006, "Thermal Conductivity Measurements of SUMMiT V Polycrystalline Silicon," Sandia Report No. SAND2006-7112, Sandia National Laboratories, Albuquerque, NM.
[18] Torczynski, J. R., Gallis, M. A., Piekos, E. S., Serrano, J. R., Phinney, L. M., and Gorby, A. D., 2008, "Validation of Thermal Models for a Prototypical MEMS Thermal Actuator," Sandia Report No. SAND2008-5749, Sandia National Laboratories, Albuquerque, NM.
[19] Saxena, S. C., and Joshi, R. K., 1989, *Thermal Accommodation and Adsorption Coefficients of Gases* (CINDAS Data Series on Material Properties Vol. II-1), C. Y. Ho, ed., Hemisphere, New York.
[20] Trott, W. M., Rader, D. J., Castañeda, J. N., Torczynski, J. R., and Gallis, M. A., 2009, "Measurement of Gas-Surface Accommodation," *Rarefied Gas Dynamics: 26th International Symposium*, American Institute of Physics, Melville, NY.

Downloaded From: https://heattransfer.asmedigitalcollection.asme.org on 06/29/2019 Terms of Use: http://www.asme.org/about-asme/terms-of-use